PHOTONICS Research

Superior multiphoton absorption properties in colloidal Mn-doped CsPbCl₃ two-dimensional nanoplatelets

Tingchao He, Junzi Li, Xin Qiu, Shuyu Xiao, and Xiaodong Lin*

College of Physics and Energy, Shenzhen University, Shenzhen 518060, China
*Corresponding author: linxd@szu.edu.cn

We have studied the two- and three-photon absorption (2PA and 3PA) properties of Mn-doped $CsPbCl_3$ two-dimensional nanoplatelets (2D NPs) and cubic nanocrystals. Compared with their cubic counterparts, the Mn-doped 2D NPs exhibit stronger quantum confinement effects that can more efficiently enhance their dopant-carrier exchange interactions and multiphoton absorption. More specifically, the maximum volume-normalized 2PA and 3PA cross sections of the 2D NPs were 6.8 and 7.2 times greater than those of their cubic counterparts, respectively, reaching up to 1237 GM/nm^3 in the visible light band and 2.24×10^{-78} $cm^6 \cdot s^2 \cdot photon^{-2}/nm^3$ in the second biological window, respectively. © 2018 Chinese Laser Press

https://doi.org/10.1364/PRJ.6.001021

1. INTRODUCTION

As members of the colloidal semiconductor nanocrystals (NCs) family, cesium lead halide perovskites in the form of $CsPbX_3$ (X represents Cl, Br, I) offer outstanding optical properties such as high photoluminescence (PL) quantum yield and defect tolerance [1–3]. Their wavelength tunability can cover the full visible spectrum through either composition or size manipulation. $CsPbX_3$ NCs are potential candidates for a variety of optoelectronic and photonic applications such as chiroptics, light-emitting diodes, photodetectors, and nonlinear optical devices [4–9].

Doping is a well-known strategy that may lead to novel functionalities and significant improvements in device efficiency. To date, various ions that have been used as dopants for $CsPbX_3$ NCs have been reported [10–12]. Among those, the doping of $CsPbX_3$ NCs with Mn^{2+} has recently attracted much attention because the presence of Mn^{2+} can introduce novel optical and magnetic features to the NCs [13,14]. For instance, the energy transfer from excitons to Mn^{2+} results in a strong emission from the field transition of Mn^{2+} at approximately 600 nm with a lifetime of ~1 ms [13,14]. The long lifetime of the PL emission can efficiently enhance the temporal discrimination of signals from the autofluorescence background [15,16]. Additionally, Mn-doped $CsPbX_3$ NCs often exhibit a superior quantum yield of their exciton emission than their undoped counterparts, thus making them attractive for many applications. Additionally, Mn-doped perovskite NCs

have been found to exhibit strong two-photon absorption (2PA) cross sections on the order of ~10^5 GM [17]. For weakly confined semiconductor NCs, whose sizes are much smaller than the exciton Bohr radius, the multiphoton absorption (MPA) cross sections scale linearly with their volume and show more efficient MPA in NCs with larger sizes [18]. When the size of the perovskite NCs is much smaller than the exciton Bohr radius, the increased quantum confinement effect may prevail over the decreased density of state, which may further enhance their MPA properties [19]. However, to date, studies of the quantum confinement-induced enhancements of MPA properties in Mn-doped perovskite NCs have not been reported.

In this study, the influences of the geometry of Mn-doped $CsPbCl_3$ NCs on their MPA properties were investigated. By performing femtosecond transient absorption (fs-TA) spectra measurements, we found that more efficient energy transfer from the excitons to Mn^{2+} can be induced in the Mn-doped $CsPbCl_3$ two-dimensional nanoplatelets (2D NPs) compared with those in their cubic counterparts. More importantly, the 2D geometry of the NCs can greatly amplify their MPA under excitation from the visible to near-infrared wavelengths. Our experimental results indicate that Mn-doped perovskite 2D NPs are better alternative materials for probes of multiphoton fluorescence lifetime imaging (FLIM) systems in light of their high MPA, long PL lifetime, and superior anti-Stokes shift.

2. EXPERIMENT

A. Sample Synthesis

The experimental conditions used for the synthesis of the Mn-doped $CsPbCl_3$ 2D NPs and cubic NCs in this study were similar to those reported in the previous literature [20]. During the fabrication of Mn-doped $CsPbCl_3$ cubic NCs, a mixture of oleylamine and HCl was first introduced in a reaction flask along with $PbCl_2$, $MnCl_2$, and other reagents. When the temperature reached 180°C, a Cs precursor was quickly injected. The heating mantle was removed, and the reaction mixture was cooled to room temperature. For the fabrication of the Mn-doped $CsPbCl_3$ 2D NPs, the experimental conditions were similar to those mentioned above. The main difference was that the Cs-to-Pb precursor ratio was 1:5 for the cubic NCs and 1:2 for the 2D NPs. The 2D NPs and cubic NCs were precipitated with acetone and redispersed in hexane. The obtained solutions were then diluted with hexane to the desired optical density for use in spectroscopic experiments. The doping concentrations of Mn^{2+} in both the 2D NPs and cubic NCs were equal and approximately 0.2%.

B. Sample Characterization

The PL quantum yields of the perovskite 2D NPs and the cubic NCs were determined using quinine sulfate monohydrate ($\eta_{350\ nm} = 0.58$) as a standard. The size and shape of the NCs were recorded using a high-resolution transmission electron microscope (HR-TEM) (JEOL, JEM-2100F) at 200 kV. The linear absorption spectra of the samples were measured using a ultraviolet–visible (UV–vis) spectrometer (Lambda 950, PerkinElmer, Inc.), while their PL spectra were measured using a fluorescence spectrophotometer (SENS-9000, Zolix).

C. Femtosecond TA Measurements

The samples were pumped at 350 nm and probed with a white-light continuum. The probe pulses (350–750 nm) were generated by focusing a small portion (∼5 μJ) of fundamental 800 nm laser pulses into a thin CaF_2 plate. The linear polarization of the pump pulse was adjusted to be perpendicular to that of the probe pulse using a polarizer and a half-wave plate. Cross-polarization helps to eliminate any early contribution from coherent artifacts. The pump-induced changes in the transmission ($\Delta T/T$) of the probe beam were monitored using a monochromator/photomultiplier configuration with lock-in detection. The pump beam was chopped at 100 Hz, which was used as the reference frequency for the lock-in amplifier.

D. Z-Scan Measurements

The MPA cross sections of the 2D NPs and the cubic NCs were measured via Z-scan measurements [21], where a beam splitter was used to divide the incident laser beam into two parts. The first part served as the reference, while the second part functioned as the signal beam. The latter was focused using a circular lens with a focal length of 30 cm into a 1 mm thick quartz cuvette filled with the sample solution. The beam transmitted through the samples that could be influenced by the MPA was detected by a signal power detector. From the open-aperture Z-scan curves, we can obtain 2PA and three-photon absorption (3PA) coefficients (α_2 and α_3) from the following equations:

$$\Delta T(2PA) = \frac{1}{1 + \alpha_2 \left(\frac{1-e^{-\alpha_0 L}}{\alpha_0}\right)\{I_0/[1 + (z/z_0)^2]\}}, \quad (1)$$

$$\Delta T(3PA) = \frac{1}{\left\{1 + 2\alpha_3 \left(\frac{1-e^{-2\alpha_0 L}}{2\alpha_0}\right)\{I_0/[1 + (z/z_0)^2]\}^2\right\}^{0.5}}, \quad (2)$$

where $\Delta T(2PA)$ and $\Delta T(3PA)$ are the normalized transmittance of the Z-scan measurements, α_0 is the linear absorption of the samples, L is the thickness of the samples, I_0 is the peak intensity, z is the sample position, $z_0 = \pi\omega_0^2/\lambda$ is the Rayleigh range, ω_0 is the beam waist at the focal point, and λ is the laser wavelength [22]. The relevant 2PA cross section (σ_2, in units of $cm^4 \cdot s$) can be calculated from the equation

$$\sigma_2 = \frac{\alpha_2 h\nu}{N_A d_0 \times 10^{-3}}, \quad (3)$$

where $h\nu$ is the photon energy of the input light beam, N_A is Avogadro's number, d_0 is the molar concentration of the samples (in units of mol/L) [23]. Accordingly, the 3PA cross section (σ_3, in units of $cm^6 \cdot s^2$) can be calculated from the equation [24]

$$\sigma_3 = \frac{\alpha_3 (h\nu)^2}{N_A d_0 \times 10^{-3}}. \quad (4)$$

E. Multiphoton-Excited PL Measurements

For the multiphoton excited PL emission measurements, fs pulses with wavelengths ranging from 620 to 700 nm and from 1300 to 1500 nm were used as the excitation sources. The signals were dispersed using a 750 mm monochromator combined with suitable filters and detected using a photomultiplier via the standard lock-in amplifier technique. Two continuously variable neutral density filters were employed to control the incident energy of the laser pulses. A short-pass filter cut at 680 nm was placed in front of the spectrometer to remove the scattered light at the excitation laser frequencies.

3. RESULTS AND DISCUSSION

The HR-TEM images of 2D NPs and cubic NCs are shown in Figs. 1(a) and 1(b). As shown in Figs. 1(c)–1(e), the 2D NPs had non-identical lateral sizes of ∼10.1 and ∼9.6 nm, while the majority of 2D NPs had a thickness of ∼3.0 nm, which corresponds to five unit cells [25]. The as-synthesized cubic NCs had a cubic geometry with an average edge length of ∼7.8 nm, as shown in Fig. 1(f). The calculated volumes were 291 nm^3 for the 2D NPs and 475 nm^3 for the cubic NCs. Figure 2(a) shows the UV-vis and PL spectra for both the 2D NPs and the cubic NCs excited at 350 nm. We found that the 2D NPs showed more obvious features of quantum confinement effects, including stronger excitonic absorption peaks and smaller Stokes shifts compared with the cubic NCs. More specifically, the first exciton absorption peaks of the 2D NPs and cubic NCs were located at 381 nm and 385 nm, respectively, indicating band-gap shifts from 3.25 to 3.22 eV, whereas their emission peaks redshifted to 395 nm and 402 nm. The observed blue-shift in the UV-vis and PL spectra of the 2D NPs can be
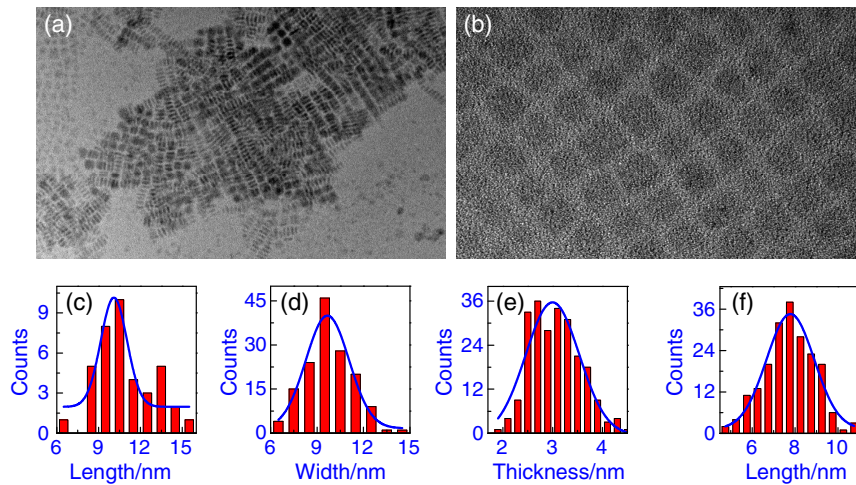
Fig. 1. HR-TEM micrographs depicting the atomic resolution of both (a) flat-lying and stacked Mn-doped $CsPbCl_3$ 2D NPs and (b) cubic NCs. Subfigures (c), (d), and (e) show the distribution of the lengths, widths, and thicknesses of the 2D NPs, respectively, while (f) shows the edge size distribution of the cubic NCs.

explained by their stronger quantum confinement effects compared with the cubic NCs [26]. Along with their excitonic PL, both the Mn-doped 2D NPs and the cubic NCs showed broad PL characteristics with peaks at ~592 nm because of the Mn^{2+} d-d transition. After absorbing the light-forming excitons, the host transfers its energy to the $^4T_1$ state of the Mn^{2+} d-electrons, followed by an emission from the $^4T_1$ to $^6A_1$ state. Additionally, the absolute quantum yields of the PL emission at ~592 nm for the 2D NPs and the cubic NCs were determined to be 2% and 16%, respectively. Compared with cubic NCs, 2D NPs exhibit much lower PL quantum yield. The 2D NPs

are strongly susceptible to surface defects due to a large surface-to-volume ratio, rendering their PL quantum yield typically quite low [27]. As shown in Fig. 2(b), their excited-state decay curves suggest that the average PL lifetime values were ~1.8 and ~1.6 ms, respectively. The long lifetime values of the Mn^{2+} d-d emissions are due to the nature of the spin-forbidden $^4T_1$ to $^6A_1$ transitions. Compared with their cubic counterpart, the 2D NPs exhibited even longer lifetimes due to their stronger quantum confinement effects.

The fs-TA spectra of the 2D NPs and the cubic NCs pumped at 350 nm are shown in Fig. 3(a). Both the 2D
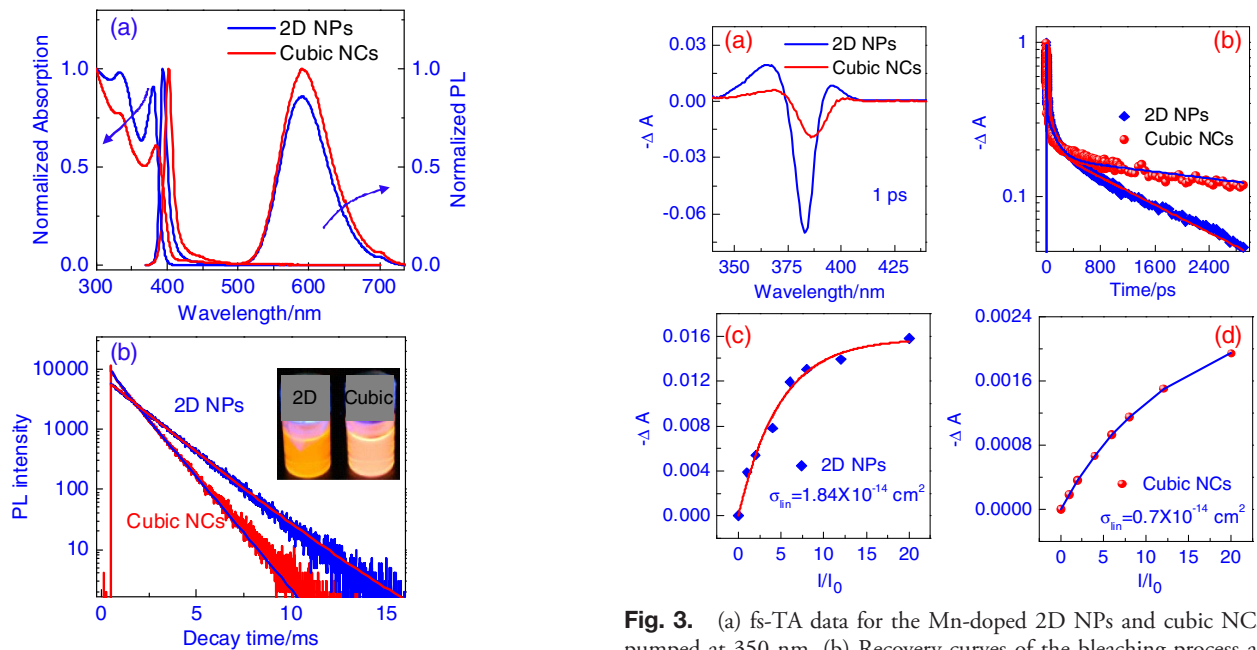
Fig. 2. (a) UV-vis absorption and PL spectra of the 2D NPs and the cubic NCs. (b) Time-dependent PL intensity of Mn^{2+} at 592 nm measured from the 2D NPs and the cubic NCs. The insets show their colloidal solutions under UV illumination ($\lambda = 365$ nm).

Fig. 3. (a) fs-TA data for the Mn-doped 2D NPs and cubic NCs pumped at 350 nm. (b) Recovery curves of the bleaching process at 383 nm for the 2D NPs and that at 387 nm for the cubic NCs. (c), (d) The excitation-intensity-dependent GSB signal amplitude at a time delay of 1 ns is shown for the 2D NPs and the cubic NCs. The curves are the best fit lines calculated based on Eq. (5).

NPs and the cubic NCs exhibited three distinctive spectral features, including ground-state bleaching (GSB) bands centered at 383 nm and 387 nm, respectively. The energies of these GSB bands are in good agreement with the lowest energy excitonic bands, and they can thus be attributed to state-filling-induced bleaching [28]. Furthermore, there are two bands of photo-induced absorption (PIA) for both the 2D NPs and cubic NCs. The short-lived PIA band at the energies just below the band gap is mostly likely derived from band-gap renormalization. The PIA band above the band gap likely corresponds to increased scattering from the photorefractive effect of the suspension.

To further explore the photophysical properties of the 2D NPs and cubic NCs, we measured their exciton–Mn^{2+} energy transfer time (τ_{ET}), which can be used to estimate the relative strength of their exciton–dopant coupling [29]. Because doping with Mn^{2+} in the host introduces an additional pathway for the depletion of excitons, the differences in exciton relaxation dynamics can reveal the exciton–dopant coupling information for the 2D NPs and cubic NCs. The τ_{ET} values were then measured by monitoring the dynamics of the exciton relaxation. Figure 3(b) shows these relevant dynamic processes near the exciton absorption peaks in the 2D NPs and cubic NCs. The recovery curves of the bleaching process for the 2D NPs and cubic NCs show three distinct components with very different time scales. The time constants (relative amplitudes) obtained via the multiexponential fitting of the fs-TA data were $\tau_1 = 5.5$ ps ($A_1 = 0.58$), $\tau_2 = 100$ ps ($A_2 = 0.21$), and 1.93 ns ($A_3 = 0.21$) for the 2D NPs and $\tau_1 = 6.2$ ps ($A_1 = 0.64$), $\tau_2 = 140$ ps ($A_2 = 0.18$), and 6.7 ns ($A_2 = 0.18$) for the cubic NCs. The fast recovery component τ_1 is attributed to the rapid electron trapping at the defects of the Cl vacancies. The second component (τ_2) represents the exciton–Mn^{2+} energy transfer, and its relative amplitude can be interpreted as the energy-transfer-related population. The nanosecond-scale recovery component (τ_3) is related to the exciton relaxation in the subpopulation of the $CsPbCl_3$ NCs, while its relative amplitude is associated with the subpopulation that does not undergo energy transfer. Comparing the exciton–Mn^{2+} energy transfer times between the 2D NPs (~100 ps) and the cubic NCs (~140 ps) suggests that the exciton–Mn^{2+} exchange coupling in the former is 1.4 times stronger than that in the latter due to its enhanced quantum confinement properties.

Then, we estimated the linear absorption cross sections (σ_{lin}) of the 2D NPs and the cubic NCs from the excitation-intensity-dependent one-photon-induced GSB signals via fs-TA spectroscopy. After fast Auger recombination within the initial hundreds of picoseconds, the samples contained only a single exciton in the subsequent time period, which is demonstrated by the parallel decay lines for all the excitation intensities after a long delay (>0.5 ns) [17]. The amplitude of the GSB signal under different excitation intensities varied based on the following equation:

$$-A(I/I_0) = -A_{max}[1 - e^{-(I/I_0)\cdot\sigma_{lin}\cdot I_0}], \qquad (5)$$

where $A(I/I_0)$ denotes the GSB signal amplitude of samples after a long time delay as a function of excitation intensity and I_0 is the minimum excitation intensity used in the fs-TA experiment [18]. As shown in Figs. 3(c) and 3(d), the

excitation-intensity-dependent GSB signal amplitude with a delay time of 1 ns could be well fitted with Eq. (5), from which the values of σ_{lin} were extracted and determined to be ~1.84×10^{-14} cm^2 for the 2D NPs and ~0.7×10^{-14} cm^2 for the cubic NCs. Correspondingly, their molar distinction coefficients were determined to be ~4.78×10^6 and ~1.82×10^6 $L\cdot cm^{-1}\cdot mol^{-1}$ at 350 nm. Additionally, compared with cubic NCs, the linear absorption cross section of the 2D NPs is considerably larger. This is the result of a higher optical field penetration in the x and y directions where the local field factor in these two directions approaches unity. For cubic NCs, the local field factor is always much smaller than 1, resulting in their much smaller linear absorption cross section [30,31].

Based on the UV-vis absorption spectra of the 2D NPs and the cubic NCs, we expected that under excitation with fs pulses in the range of 450–800 nm, they might exhibit 2PA behavior. Figure 4(a) shows the PL spectra of the 2D NPs and the cubic NCs under excitation with fs pulses at 680 nm. We found that the emission spectra of Mn^{2+} were indistinguishable from those obtained under excitation at 350 nm, indicating that the same emissive states were involved under excitation of both 350 nm and 680 nm. Although both the Mn-doped 2D NPs and NCs exhibited strong exciton emission under one-photon excitation, their emission was completely quenched under two-photon excitation, and only the emission from Mn^{2+} was observed. This implies that there are large differences between the cross sections of the $CsPbCl_3$ host and the Mn^{2+} under one- and two-photon excitation [32]. To explore whether the observed PL of the 2D NPs and the cubic NCs originated from 2PA processes, their PL intensities were measured under different excitation intensities. As shown in Fig. 4(b), the clear square relationship between the PL and excitation intensities
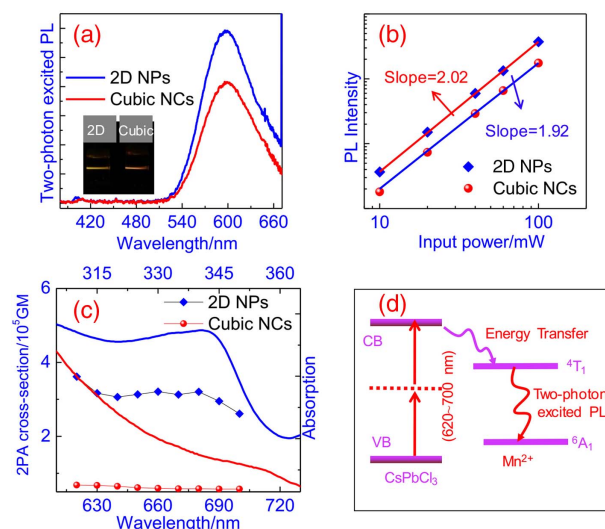
Fig. 4. (a) PL spectra for the 2D NPs and cubic NCs excited by fs pulses at 680 nm. The inset shows the PL emissions of the 2D NPs and cubic NCs. (b) PL intensity versus excitation intensity with log–log plot slopes of 1.95 and 2.02, respectively. (c) 2PA and linear absorption spectra of the 2D NPs and cubic NCs plotted over the two- and one-photon energies. (d) Photo-induced energy transfer process from the host ($CsPbCl_3$) to Mn^{2+} in the Mn-doped 2D NPs and cubic NCs under two-photon excitation.

suggests that 2PA mechanisms are truly responsible for the PL of the 2D NPs and cubic NCs [33]. Additionally, we easily observed two-photon excited PL with the naked eye in solutions of the 2D NPs and cubic NCs under excitation with a power intensity of several gigawatts per centimeter squared (GW/cm^2), as shown in the inset of Fig. 4(a). Z-scan measurements were then carried out to quantitatively determine the relevant 2PA spectra of the 2D NPs and the cubic NCs, as presented in Fig. 4(c). Excitation wavelengths in the range of 620–700 nm were chosen to gain insight into the contributions of the electronic confinement to the 2PA cross sections from wavelengths that were resonant to one-photon excitonic transitions up to the 2D continuum. For comparison, the corresponding linear absorption spectra are plotted over their one-photon energies. For the cubic NCs, a weaker contribution of the first excitonic resonance to the 2PA spectrum due to weak selection rules in the continuum was found in comparison to the energies of the quasi-continuum, which have been reported for many other semiconductor NCs [19]. In contrast, the 2PA signals for the 2D NPs showed a dominant peak at 381 nm. The similarity between the peak positions and full width at half-maximum of the linear absorption and the 2PA spectrum clearly confirms the excitonic enhancement of the 2PA process, which should also be induced by strong quantum confinement effects [34]. Analyzing the 2PA spectra of the 2D NPs and the cubic NCs shown in Fig. 4(c) shows that there is a shape dependence for the 2D NPs and the cubic NCs. The 2D NPs showed a maximum 2PA cross section of 3.6×10^5 GM at 620 nm, while that for the cubic NCs was 0.87×10^5 GM at 620 nm. Compared with cubic NCs, the 2D NPs displayed a much larger 2PA over the entire measured wavelength range, which is attributed to the confinement-related increase of the transition dipole moments and band mixing [35–37]. Since the thickness (3 nm) of the 2D NPs is much smaller than the Bohr excitonic diameter of $CsPbCl_3$ (5 nm), strong quantum confinement can be induced in the 2D NPs, which can result in the quasi-2D colloidal quantum-well-type structure experienced by the charge carriers. In turn, this significantly enhances the 2PA of the 2D NPs.

Having demonstrated the strong 2PA from the 2D NPs and cubic NCs in the visible light band, we move forward to investigate their MPA in the second biological window (1000–1700 nm), which could offer even greater advantages [38,39]. The PL properties of the 2D NPs and the cubic NCs were measured using fs pulses at 1300 nm. As expected, the obtained PL spectra of Mn^{2+} were similar to those obtained under the one-photon excitation, as shown in Fig. 5(a). Moreover, we also plotted the relationships between up-converted PL intensity and excitation intensity in Fig. 5(b). Unexpectedly, the PL intensities of both the 2D NPs and the cubic NCs had a cubic dependence on the excitation intensity, confirming that the observed PL was induced by 3PA [33]. Although the host $CsPbCl_3$ may exhibit four-photon absorption at 1 nm, the observed PL at 592 nm was not induced by four-photon excited energy transfer from the host to the Mn^{2+} and subsequent $^4T_1$ – $^6A_1$ Mn d-electron emission; otherwise, a fourth-power dependence would have been observed. Additionally, we found that the four-photon excited PL emission of the 2D NPs and cubic NCs made
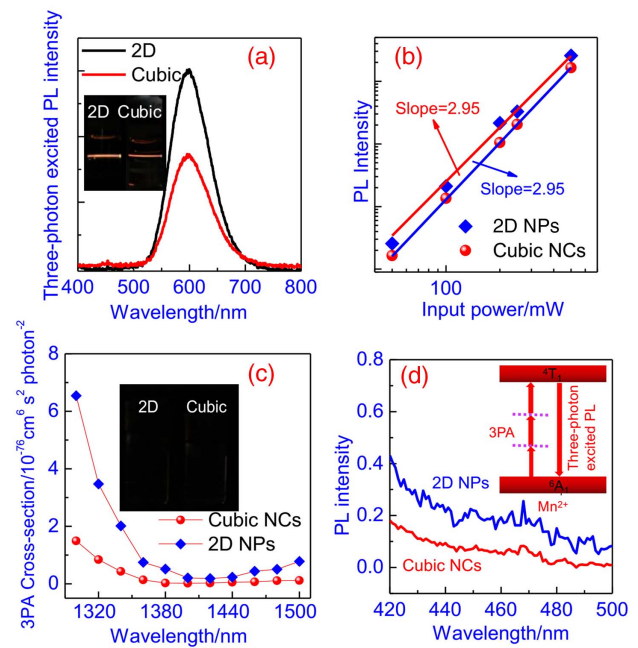
Fig. 5. (a) PL spectra for the 2D NPs and cubic NCs excited by fs pulses at 1300 nm. The inset shows the PL emissions of the Mn-doped 2D NPs and cubic NCs. (b) PL intensity of the 2D NPs and cubic NCs versus the optical intensity with log–log plot slopes of 2.98 and 3.02, respectively. (c) 3PA spectra of the 2D NPs and cubic NCs. The inset shows solutions of the 2D NPs and cubic NCs in a pure host ($CsPbCl_3$) under the same excitation intensity used for the inset of (a). (d) One-photon excitation spectra of the 2D NPs and cubic NCs detected at 592 nm. The inset shows the direct 3PA process from the $^6A_1$ state to the $^4T_1$ state in the Mn^{2+} of the 2D NPs and cubic NCs.

of undoped $CsPbCl_3$ was difficult to measure under the same excitation intensity, as shown in the inset of Fig. 5(c). Therefore, the underlying PL mechanism for the Mn^{2+} emission at 592 nm was attributed to direct 3PA transitions from the $^6A_1$ state to the $^4T_1$ state of Mn^{2+}, as shown in Fig. 5(d). The 3PA spectra of the 2D NPs and the cubic NCs were then measured using the Z-scan measurements. While tuning the excitation wavelength from 1500 to 1300 nm, the 3PA cross sections of the 2D NPs and the cubic NCs continuously increased, as shown in Fig. 5(c). The maximum 3PA cross sections of the Mn-doped NPs and NCs were 6.54×10^{-76} and 1.49×10^{-76} $cm^6 \cdot s^2 \cdot photon^{-2}$ at 1300 nm, respectively. Compared with the cubic NCs, it can be seen that the maximum 3PA cross section of the 2D NPs was again larger due to their stronger quantum confinement effects. To further confirm the possibility of such a transition, we measured the linear excitation spectra of the 2D NPs and cubic NCs detected at 592 nm. As shown in Fig. 5(d), a very weak PL emission at 592 nm was obtained under excitation wavelengths ranging from 420 to 500 nm, which were likely induced by the direct one-photon transitions of the $^6A_1$ state to the $^4T_1$ state but not by the excitonic energy transferred from the host to the Mn^{2+}. The 3PA spectra of the 2D NPs and the cubic NCs resembled their linear excitation spectra, providing supporting evidence for the direct 3PA transition from the $^6A_1$ state to the $^4T_1$ state.
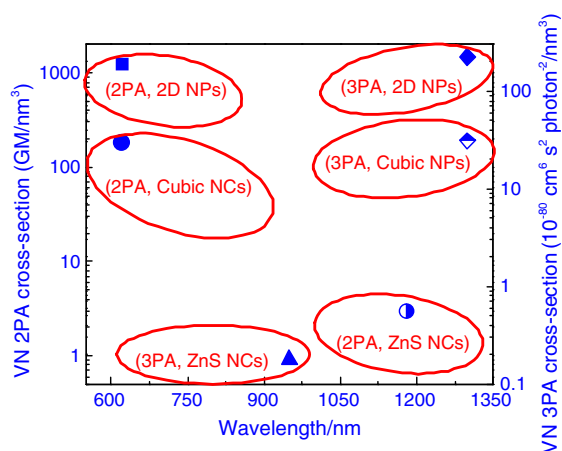
Fig. 6. Comparison of the maximum VN 2PA and 3PA cross sections of Mn-doped $CsPbCl_3$ 2D NPs and cubic NCs, as well as Mn-doped ZnS spherical NCs.

In addition to the absolute MPA cross section of the NCs, we also calculated the maximum volume-normalized (VN) MPA cross sections, which yield more intrinsic values, to study the influences of geometry on the MPA [19,37]. As shown in Fig. 6, the maximum VN 2PA cross sections of the 2D NPs and cubic NCs are determined to be 1237 GM/nm^3 and 183 GM/nm^3, respectively, while the relevant values of the 3PA cross sections are 2.24×10^{-78} $cm^6 \cdot s^2 \cdot photon^{-2}/nm^3$ and 3.1×10^{-79} $cm^6 \cdot s^2 \cdot photon^{-2}/nm^3$, respectively. Additionally, the relevant values for the Mn-doped ZnS spherical NCs were also added for comparison purposes. Compared with their cubic counterparts, the 2D geometry of the Mn-doped $CsPbCl_3$ NPs led to VN 2PA and 3PA values that were 6.8 and 7.2 times larger, respectively, due to the stronger confinement-related increases of the transition dipole moments and band mixing. Additionally, the VN 2PA and 3PA cross sections of the Mn-doped $CsPbCl_3$ 2D NPs and cubic NCs were 1–3 orders of magnitude larger than those of the Mn-doped ZnS spherical NCs [40,41], which can be ascribed to the stronger quantum confinement effects of the $CsPbCl_3$ 2D NPs.

4. CONCLUSION

In summary, we synthesized Mn-doped $CsPbCl_3$ 2D NPs and cubic NCs for comparative purposes. Their linear absorption cross sections and the strengths of their exciton–dopant couplings were investigated via fs-TA spectroscopy. Most importantly, we determined that the strong quantum confinement effects of the 2D NPs can be used to enhance their MPA. Our broadband Z-scan measurements show that the 2D NPs exhibit much better MPA from the visible light band to the second biological window compared to their cubic counterparts. Additionally, we confirmed that the MPA mechanisms of the 2D NPs and cubic NCs for the excitation wavelengths in the 620–700 nm and 1300–1500 nm ranges can be attributed to two-photon excited excitonic energy transfer from the host to the Mn^{2+} and direct 3PA transition from the $^6A_1$ state to the $^4T_1$ state, respectively.

REFERENCES

1. L. Protesescu, S. Yakunin, M. I. Bodnarchuk, F. Krieg, R. Caputo, C. H. Hendon, R. X. Yang, A. Walsh, and M. V. Kovalenko, "Nanocrystals of cesium lead halide perovskites ($CsPbX_3$, X=Cl, Br, and I): novel optoelectronic materials showing bright emission with wide color gamut," Nano Lett. **15**, 3692–3696 (2015).
2. Q. A. Akkerman, G. Rainò, M. V. Kovalenko, and L. Manna, "Genesis, challenges and opportunities for colloidal lead halide perovskite nanocrystals," Nat. Mater. **17**, 394–405 (2018).
3. J. Kang and L. Wang, "High defect tolerance in lead halide perovskite $CsPbBr_3$," J. Phys. Chem. Lett. **8**, 489–493 (2017).
4. T. He, J. Li, X. Li, C. Ren, Y. Luo, F. Zhao, R. Chen, X. Lin, and J. Zhang, "Spectroscopic studies of chiral perovskite nanocrystals," Appl. Phys. Lett. **111**, 151102 (2017).
5. X. Li, Y. Wu, S. Zhang, B. Cai, Y. Cui, J. Song, and H. Zeng, "$CsPbX_3$ quantum dots for lighting and displays: room-temperature synthesis, photoluminescence superiorities, underlying origins and white light-emitting diodes," Adv. Funct. Mater. **26**, 2435–2445 (2016).
6. J. Chen, P. Chábera, T. Pascher, M. E. Messing, R. Schaller, S. Canton, K. Zheng, and T. Pullerits, "Enhanced size selection in two-photon excitation for $CsPbBr_3$ perovskite nanocrystals," J. Phys. Chem. Lett. **8**, 5119–5124 (2017).
7. Y. Wang, X. Li, X. Zhao, L. Xiao, H. Zeng, and H. Sun, "Nonlinear absorption and low-threshold multiphoton pumped stimulated emission from all-inorganic perovskite nanocrystals," Nano Lett. **16**, 448–453 (2016).
8. X. X. Sheng, G. Y. Chen, C. Wang, W. Q. Wang, J. F. Hui, Q. Zhang, K. H. Yu, W. Wei, M. D. Yi, M. Zhang, Y. Deng, P. Wang, X. X. Xu, Z. H. Dai, J. C. Bao, and X. Wang, "Polarized optoelectronics of $CsPbX_3$ (X = Cl, Br, I) perovskite nanoplates with tunable size and thickness," Adv. Funct. Mater. **28**, 1800283 (2018).
9. J. Li, C. Ren, X. Qiu, X. Lin, R. Chen, C. Yin, and T. He, "Ultrafast optical nonlinearity of blue-emitting perovskite nanocrystals," Photon. Res. **6**, 554–559 (2018).
10. D. Parobek, B. J. Roman, Y. Dong, H. Jin, E. Lee, M. Sheldon, and D. H. Son, "Exciton-to-dopant energy transfer in Mn-doped cesium lead halide perovskite nanocrystals," Nano Lett. **16**, 7376–7380 (2016).
11. A. Swarnkar, V. Kumar Ravi, and A. Nag, "Beyond colloidal cesium lead halide perovskite nanocrystals: analogous metal halides and doping," ACS Energy Lett. **2**, 1089–1098 (2017).
12. J. Yao, J. Ge, B. Han, K. Wang, H. Yao, H. Yu, J. Li, B. Zhu, J. Song, C. Chen, Q. Zhang, H. Zeng, Y. Luo, and S. Yu, "Ce^{3+}-doping to modulate photoluminescence kinetics for efficient $CsPbBr_3$ nanocrystals based light-emitting diodes," J. Am. Chem. Soc. **140**, 3626–3634 (2018).
13. J. Zhu, X. Yang, Y. Zhu, Y. Wang, J. Cai, J. Shen, L. Sun, and C. Li, "Room-temperature synthesis of Mn-doped cesium lead halide quantum dots with high Mn substitution ratio," J. Phys. Chem. Lett. **8**, 4167–4171 (2017).
14. W. J. Mir, M. Jagadeeswararao, S. Das, and A. Nag, "Colloidal Mn-doped cesium lead halide perovskite nanoplatelets," ACS Energy Lett. **2**, 537–543 (2017).
15. T. He, C. Ren, Z. Li, S. Xiao, J. Li, X. Lin, C. Ye, J. Zhang, L. Guo, W. Hu, and R. Chen, "Thermally activated delayed fluorescence organic dots for two-photon fluorescence lifetime imaging," Appl. Phys. Lett. **112**, 211102 (2018).
16. P. Wu and X. Yan, "Doped quantum dots for chemo/biosensing and bioimaging," Chem. Soc. Rev. **42**, 5489–5521 (2013).
17. T. He, J. Li, C. Ren, S. Xiao, Y. Li, R. Chen, and X. Lin, "Strong two-photon absorption of Mn-doped $CsPbCl_3$ perovskite nanocrystals," Appl. Phys. Lett. **111**, 211105 (2017).

18. J. Chen, K. Žídek, P. Chábera, D. Liu, P. Cheng, L. Nuuttila, M. J. Al-Marri, H. Lehtivuori, M. E. Messing, K. Han, K. Zheng, and T. Pullerits, "Size- and wavelength-dependent two-photon absorption cross-section of $CsPbBr_3$ perovskite quantum dots," J. Phys. Chem. Lett. **8**, 2316–2321 (2017).

19. R. Scott, A. W. Achtstein, A. Prudnikau, A. Antanovich, S. Christodoulou, I. Moreels, M. Artemyev, and U. Woggon, "Two photon absorption in II-VI semiconductors: the influence of dimensionality and size," Nano Lett. **15**, 4985–4992 (2015).

20. S. Das Adhikari, S. K. Dutta, A. Dutta, A. K. Guria, and N. Pradhan, "Chemically tailoring the dopant emission in manganese-doped $CsPbCl_3$ perovskite nanocrystals," Angew. Chem. (Int. Ed.) **56**, 8746–8750 (2017).

21. M. Sheik-Bahae, A. A. Said, T.-H. Wei, D. J. Hagan, and E. W. Van Stryland, "Sensitive measurement of optical nonlinearities using a single beam," IEEE J. Quantum Electron. **26**, 760–769 (1990).

22. R. S. S. Kumar, S. V. Rao, L. Giribabu, and D. N. Rao, "Femtosecond and nanosecond nonlinear optical properties of alkyl phthalocyanines studied using Z-scan technique," Chem. Phys. Lett. **447**, 274–278 (2007).

23. G. S. He, G. C. Xu, P. N. Prasad, B. A. Reinhardt, J. C. Bhatt, and A. G. Dillard, "Two-photon absorption and optical-limiting properties of novel organic compounds," Opt. Lett. **20**, 435–437 (1995).

24. G. S. He, J. D. Bhawalkar, P. N. Prasad, and B. A. Reinhardt, "Three-photon-absorption-induced fluorescence and optical limiting effects in an organic compound," Opt. Lett. **20**, 1524–1526 (1995).

25. I. Levchuk, A. Osvet, X. Tang, M. Brandl, J. D. Perea, F. Hoegl, G. J. Matt, R. Hock, M. Batentschuk, and C. J. Brabec, "Brightly luminescent and color-tunable formamidinium lead halide perovskite $FAPbX_3$ (X = Cl, Br, I) colloidal nanocrystals," Nano Lett. **17**, 2765–2770 (2017).

26. Y. Dong, T. Qiao, D. Kim, D. Parobek, D. Rossi, and D. H. Son, "Precise control of quantum confinement in cesium lead halide perovskite quantum dots via thermodynamic equilibrium," Nano Lett. **18**, 3716–3722 (2018).

27. B. J. Bohn, Y. Tong, M. Gramlich, M. L. Lai, M. Döblinger, K. Wang, R. L. Z. Hoye, P. Müller-Buschbaum, S. D. Stranks, A. S. Urban, L. Polavarapu, and J. Feldmann, "Boosting tunable blue luminescence of halide perovskite nanoplatelets through postsynthetic surface trap repair," Nano Lett. **18**, 5231–5238 (2018).

28. J. Butkus, P. Vashishtha, K. Chen, J. K. Gallaher, S. K. K. Prasad, D. Z. Metin, G. Laufersky, N. Gaston, J. E. Halpert, and J. M. Hodgkiss, "The evolution of quantum confinement in $CsPbBr_3$ perovskite nanocrystals," Chem. Mater. **29**, 3644–3652 (2017).

29. D. Rossi, D. Parobek, Y. Dong, and D. H. Son, "Dynamics of exciton-Mn energy transfer in Mn-doped $CsPbCl_3$ perovskite nanocrystals," J. Phys. Chem. C **121**, 17143–17149 (2017).

30. A. W. Achtstein, A. Antanovich, A. Prudnikau, R. Scott, U. Woggon, and M. Artemyev, "Linear absorption in CdSe nanoplates: thickness and lateral size dependency of the intrinsic absorption," J. Phys. Chem. C **119**, 20156–20161 (2015).

31. T. He, J. Li, X. Qiu, S. Xia, C. Yin, and X. Lin, "Highly enhanced normalized-volume multiphoton absorption in $CsPbBr_3$ 2D nanoplates," Adv. Opt. Mater. **2018**, 1800843 (2018).

32. T. He, R. Chen, Z. B. Lim, D. Rajwar, L. Ma, Y. Wang, Y. Gao, A. C. Grimsdale, and H. Sun, "Efficient energy transfer under two-photon excitation in a 3D, supramolecular, Zn(II)-coordinated, self-assembled organic network," Adv. Opt. Mater. **2**, 40–47 (2014).

33. G. S. He, L. S. Tan, Q. Zheng, and P. N. Prasad, "Multiphoton absorbing materials: molecular designs, characterizations, and applications," Chem. Rev. **108**, 1245–1330 (2008).

34. C. Huang, Y. G. Shuai, W. Zhang, N. Yia, S. Xiao, and Q. Song, "Giant blueshifts of excitonic resonances in two-dimensional lead halide perovskite," Nano Energy **41**, 320–326 (2017).

35. O. Saouma, C. C. Stoumpos, J. Wong, M. G. Kanatzidis, and J. I. Jang, "Selective enhancement of optical nonlinearity in two-dimensional organic-inorganic lead iodide perovskites," Nat. Commun. **8**, 742 (2017).

36. A. W. Achtstein, A. Ballester, J. L. Movilla, J. Hennig, J. I. Climente, A. Prudnikau, A. Antanovich, R. Scott, M. V. Artemyev, J. Planelles, and U. Woggon, "One- and two-photon absorption in CdS nanodots and wires: the role of dimensionality in the one- and two-photon luminescence excitation spectrum," J. Phys. Chem. C **119**, 1260–1267 (2015).

37. L. A. Padilha, G. Nootz, P. D. Olszak, S. Webster, D. J. Hagan, E. W. Van Stryland, L. Levina, V. Sukhovatkin, L. Brzozowski, and E. H. Sargent, "Optimization of band structure and quantum-size-effect tuning for two-photon absorption enhancement in quantum dots," Nano Lett. **11**, 1227–1231 (2011).

38. A. K. Mandal, S. Sreejith, T. He, S. K. Maji, X. Wang, S. L. Ong, J. Joseph, H. Sun, and Y. Zhao, "Three-photon-excited luminescence from unsymmetrical cyanostilbene aggregates: morphology tuning and targeted bioimaging," ACS Nano **9**, 4796–4805 (2015).

39. J. Qian, D. Wang, F. Cai, W. Xi, L. Peng, Z. Zhu, H. He, M. Hu, and S. He, "Observation of multiphoton-induced fluorescence from graphene oxide nanoparticles and applications in vivo functional bioimaging," Angew. Chem. (Int. Ed.) **51**, 10570–10575 (2012).

40. R. Subha, V. Nalla, J. H. Yu, S. W. Jun, K. Shin, T. Hyeon, C. Vijayan, and W. Ji, "Efficient photoluminescence of Mn^{2+}-doped ZnS quantum dots excited by two-photon absorption in near-infrared window II," J. Phys. Chem. C **117**, 20905–20911 (2013).

41. J. H. Yu, S. Kwon, Z. Petrášek, O. K. Park, S. Woojoo Jun, K. Shin, M. Choi, Y. Il Park, K. Park, H. B. Na, N. Lee, D. W. Lee, J. H. Kim, P. Schwille, and T. Hyeon, "High-resolution three-photon biomedical imaging using doped ZnS nanocrystals," Nat. Mater. **12**, 359–366 (2013).